

The Goldilocks problem of the quasar contribution to reionization

Enrico Garaldi,¹★† Michele Compostella,^{2,3} and Cristiano Porciani¹

¹Argelander Institut für Astronomie der Universität Bonn, Auf dem Hügel 71, 53121 Bonn, Germany

²Max Planck Institute for Astrophysics, Karl-Schwarzschild Straße 1, 85741 Garching, Germany

³Max Planck Computing and Data Facility, Gießenbachstraße 2, 85741 Garching, Germany

Accepted XXX. Received YYY; in original form ZZZ

ABSTRACT

The detection of an unexpectedly large number of faint candidate quasars (QSO) at $z \gtrsim 4$ has motivated Madau and Haardt to investigate a reionization scenario in which active galactic nuclei dominate the photon budget at all times. Their analytical study reveals that this picture is in agreement with the evolution of the HI volume fraction in the intergalactic medium (IGM) and the optical depth to Thomson scattering of the cosmic microwave background. We employ a suite of hydrodynamical simulations post-processed with a radiative transfer code to further investigate the properties of such a reionization history. In particular, we generate synthetic absorption-line spectra for HI and He II that we compare with observational data. Although we confirm the analytical results mentioned above, we also find that the evolution of the IGM temperature and of the He II optical depth are at odds with current observational constraints. Nevertheless, the QSO-dominated scenario presents the attractive feature that it naturally generates an inhomogeneous IGM and thus produces an extended tail at high values in the distribution function of the HI effective optical depth, in agreement with recent observations. We find tentative evidence that considering some QSO emission at redshift $z \gtrsim 5$ could reconcile such observations with numerical simulations that have so far failed to reproduce this feature. Finally, we show that collecting more He II-absorption spectra at $z \gtrsim 3$ and studying their distinctive characteristics will be key to precisely constraining the QSO contribution to reionization.

Key words: radiative transfer – intergalactic medium – cosmology:theory – large-scale structure of the Universe – quasars:general

1 INTRODUCTION

Over the last decades, a standard picture has emerged for the epoch of cosmic reionization (EoR, see e.g. Zaroubi 2013; McQuinn 2016 for a review). In this scenario, ultraviolet (UV) radiation produced by star formation in faint galaxies is responsible for the ionization of hydrogen and for the first ionization of helium in the intergalactic medium (IGM) at redshift $6 \lesssim z \lesssim 10$. Later on, at $2 \lesssim z \lesssim 4$, harder radiation from quasars (QSOs) causes the second ionization of the diffuse helium.

This standard picture is supported by observations and theoretical considerations. The rapid evolution in the transmission of the Lyman- α ($\text{Ly}\alpha$) forest at $z \lesssim 6$ (Fan et al. 2006; Becker et al. 2013, 2015), and the drop in the number density of $\text{Ly}\alpha$ emitters and $\text{Ly}\alpha$ -bright galaxies at $6 < z < 7$ (Ota et al. 2010; Pentericci et al. 2011; Shibuya et al. 2012; Furusawa et al. 2016; Mason et al. 2018; but see Sadoun et al. 2017) set constraints on the timing of hydrogen reionization which are also supported by the

latest data on the Thomson optical depth of the cosmic microwave background (CMB, Planck Collaboration et al. 2016b, 2018). Similarly, the He II $\text{Ly}\alpha$ forest encodes information about ‘helium reionization’, a conventional name used to indicate the transition from He II to He III. Although only a handful of ‘clean’ sightlines (with little foreground absorption down to the He II $\text{Ly}\alpha$ resonance wavelength) are available, they consistently show a rapid increase in the transmitted flux between $2.7 \lesssim z \lesssim 3$ (Shull et al. 2010; Furlanetto & Dixon 2010; Worseck et al. 2011, 2016, 2018). Further constraints can be obtained from the evolution of the IGM temperature at mean density, inferred from the HI $\text{Ly}\alpha$ absorption features. Observational data are available only at $z \lesssim 5$ and show a large scatter, partially reflecting the different data analysis techniques used to retrieve this information (e.g. Rorai et al. 2018; Boera et al. 2018; Hiss et al. 2018; Walther et al. 2018). Nevertheless, the peak at $z \approx 3$ is usually interpreted as a signature of the completion of helium reionization.

Still, many details of the EoR are loosely constrained and there is space for substantial modifications to accommodate recent observations that challenge the standard description. The spectrum of the quasar ULAS J0148+0600 (Becker et al. 2015) contains a particularly long ($\sim 110 h^{-1}$ Mpc) Gunn-Peterson trough at redshift

★ egaraldi@uni-bonn.de

† Member of the International Max Planck Research School (IMPRS) for Astronomy and Astrophysics at the Universities of Bonn and Cologne

$z = 5.98$, which appears at odds with a standard reionization history (e.g. Chardin et al. 2017) and may suggest an incomplete hydrogen reionization (Kulkarni et al. 2018). More recently, Barnett et al. (2017) observed a very extended dark gap covering the range $6.12 < z < 7.04$ and corresponding to a comoving length of $240 h^{-1}$ Mpc with a mean HI fraction $> 10^{-4}$. Additionally, current models of reionization have difficulties to explain the IGM inhomogeneity indicated by the broad probability distribution of the HI optical depth observed at $5 \lesssim z \lesssim 6$ (Becker et al. 2015; Bosman et al. 2018; Eilers et al. 2018; but see Gnedin et al. 2017). Several studies have addressed this problem and indicated possible solutions. It has emerged that opacity fluctuations can be enhanced either in the presence of local temperature variations (D’Aloisio et al. 2015) or by considering that the mean free path (λ_{mfp}) of ionizing photons depends on the local photoionization rate (Davies & Furlanetto 2016; Becker et al. 2018). Another possibility is to consider a scenario in which the QSO contribution to the reionization photon budget is boosted at high redshift (Chardin et al. 2017). This is the direction we explore in this paper.

The rationale for our investigation lies in an ongoing discussion in the literature regarding the abundance of faint active galactic nuclei at high redshift and their role during the EoR. By applying a novel selection criterion within a deep field with extensive multiwavelength coverage, Giallongo et al. (2015) have detected an unexpectedly large number of faint (i.e. with an absolute magnitude $M_{\text{AB}} \sim -20$ at 1450 \AA) QSO candidates at $z > 4$ (but see Ricci et al. 2017; McGreer et al. 2018; Parsa et al. 2018; Kulkarni et al. 2018). If confirmed, this result would suggest that QSOs provide an important contribution to the photon budget during the entire EoR and, possibly, even dominate it. Inspired by these findings, Madau & Haardt (2015, MH hereafter) have built an analytical model for the EoR in which all ionizing photons are generated by QSOs. Interestingly, the results of the model satisfy the observational constraints on the evolution of the HII fraction and on the Thomson optical depth of CMB photons. Following Giallongo et al. (2015) and MH, a number of authors have revisited the question of the importance of non-stellar sources during hydrogen reionization (e.g. D’Aloisio et al. 2017a; Upton Sanderbeck et al. 2016; Chardin et al. 2017; Onoue et al. 2017; Kulkarni et al. 2017; Qin et al. 2017; Mitra et al. 2018; Hassan et al. 2018). However, these analytic or semi-numerical studies do not include a detailed treatment of radiation transfer which is necessary to make more accurate predictions (especially for the temperature of the IGM) and produce realistic synthetic observations to be compared with actual data. On the other hand, the investigations based on fully-coupled radiation-hydrodynamical simulations consider rather small computational volumes and thus suffer from sample variance. In this work, we improve upon existing results by performing detailed hydrodynamical simulations of a scenario in which cosmic reionization is driven only by quasars. We use a suite of large simulation boxes post-processed with a radiative-transfer (RT) code in order to track the detailed evolution of the IGM. We then produce realistic synthetic observations and use them to (i) test the plausibility of the QSO-only reionization model, (ii) characterise the impact of the QSO contribution on the Lyman- α forest, and (iii) provide predictions for a number of observables that should be able to discriminate between the standard reionization scenario and a QSO-dominated one. Such information is extremely valuable in order to disentangle the role of different types of sources and shed light on the properties of the high-redshift IGM.

The paper is organized as follows. In Section 2, we describe our numerical techniques and the specifics of the runs. The simu-

lation outputs are presented in Section 3 and analysed in Section 4 where we discuss several mock observations that we compare with actual data and previous theoretical work. Finally, we summarise our findings and draw conclusions in Section 5.

2 NUMERICAL METHODS

In this Section, we describe the setup of our numerical simulations, together with the modelling of the radiation sources and their calibration against recent observations. The techniques we use here are based on Compostella et al. (2013, hereafter CCP1) and Compostella et al. (2014, CCP2), to which we refer for further details.

2.1 Hydrodynamical simulations

We consider a flat Λ CDM cosmological model and use the results of the *Planck* satellite to fix the parameters that determine its background evolution and the power spectrum of the Gaussian linear perturbations (Planck Collaboration et al. 2016a). For the present-day values of the matter density, the baryon density and the Hubble parameter we thus use $\Omega_{\text{m}} = 0.306$, $\Omega_{\text{b}} = 0.0483$ and $H_0 = 67.9 \text{ km s}^{-1} \text{ Mpc}^{-1}$, respectively. Moreover, the normalization of the linear power spectrum and the primordial spectral index are $\sigma_8 = 0.815$ and $n = 0.958$.

We run four hydrodynamical simulations using the adaptive mesh refinement (AMR) code RAMSES (Teyssier 2002) and employing a cubic box of comoving side $L_{\text{box}} = 100 h^{-1}$ Mpc with periodic boundary conditions. The dark matter (DM) is sampled using 256^3 particles (corresponding to a particle mass $m_{\text{DM}} = 4.3 \times 10^9 h^{-1} M_{\odot}$) while the hydrodynamical equations are solved on a base grid of 256^3 elements with up to 7 levels of refinement. This way, the simulations reach a maximum nominal resolution of approximately $3 h^{-1}$ kpc and resolve the Jeans length of the gas with several computational mesh cells. The refinement strategy is quasi-Lagrangian, namely a cell is split whenever the enclosed mass exceeds the critical threshold of $8 m_{\text{DM}}$. The initial conditions are produced using the GRAFIC package (Bertschinger 2001). The gas is assumed to follow an ideal equation of state with adiabatic index $\gamma = 5/3$ and has a primordial composition (i.e. the helium mass fraction is $Y = 0.24$). We do not track star formation and neglect stellar feedback since the scales of interest for the analysis of the EoR are much larger than those affected by such phenomena (see also CCP1, CCP2). This approximation may somewhat enhance the occurrence of dense systems that act as sinks of radiation. Note that our simulations do not include a background of UV radiation. The reason is twofold. First, we do not consider ionizing photons emitted by stars. Second, the ionizing radiation produced by QSOs is treated in post-processing as described in Section 2.2.

DM haloes are identified using the HOP finder (Eisenstein & Hut 1998) in its default configuration. We only consider haloes containing more than 70 DM particles (corresponding to halo masses $M_{\text{h}} > 3 \times 10^{11} h^{-1} M_{\odot}$) whose abundance agrees well with popular fitting functions (e.g. Jenkins et al. 2001).

2.2 Radiative transfer

Modelling the timing and the properties of the EoR requires an accurate treatment of RT. This consists of two parts: describing the properties of the sources of UV radiation and propagating the ionizing photons through the IGM.

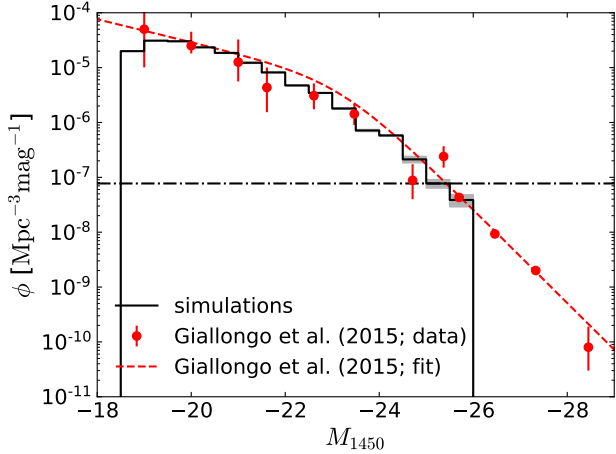


Figure 1. The QLF, ϕ , constructed from our simulations (solid histogram) is compared with the observational results by Giallongo et al. (2015, points with errorbars) and the best-fit double power law reported in the same work (dashed line). The shaded regions show the rms scatter of the four simulations around the mean. The horizontal dot-dashed line highlights the value of ϕ corresponding to one object per simulation box and magnitude bin.

2.2.1 Ionizing sources

The spatial distribution of the ionizing sources within the cosmic web influences the development of cosmic reionization. Having the possibility to model this effect in a realistic way represents one of the main advantages of numerical simulations with respect to analytical models that describe radiation as a uniform background. In order to assign a position to each source of radiation, we assume that QSOs reside at the centre of DM haloes (neglecting multiple occupancies) and that their luminosity scales (statistically) with the mass of the host haloes (e.g. Silk & Rees 1998; Wyithe & Loeb 2002; Volonteri & Rees 2006; Compostella et al. 2013, 2014). Several observations support this hypothesis (e.g. Kim et al. 2009; Cantalupo et al. 2012; Morselli et al. 2014; Ota et al. 2018; Onoue et al. 2018) although some exceptions have been found (Bañados et al. 2013; Fanidakis et al. 2013; Mazzucchelli et al. 2017). In practice, we consider each DM halo as a potential host of a QSO and sample the associated magnitude at 1450 Å (M_{AB}) from a Gaussian distribution with mean

$$M_{AB} = -\frac{10}{3} \log \left(\frac{M_h}{h^{-1} M_\odot} \right) + \varepsilon \quad (1)$$

and standard deviation σ_{AB} . We determine the free parameters ε and σ_{AB} by fitting the shape of the quasar luminosity function (QLF) measured by Giallongo et al. (2015) at redshift $4.0 < z < 4.5$. Using 1000 realisations of the QSO assignment, we obtain $\varepsilon = 19$ and $\sigma_{AB} = 1.25$ (with some freedom within a degeneracy region in parameter space). This implies that the resolved haloes in our simulations host QSOs in the range $-25.76 \leq M_{AB} \leq -18.67$. Our ionizing sources thus sample the faint end of the QLF which generates the majority of the ionising photons (only 11.6 per cent of the total should be emitted by the unresolved faint sources).

We employ a lightbulb model to describe the QSO activity. Sources are randomly switched on with a probability that is independent of the properties of the host halo. Once activated, a QSO has a constant emissivity for a lifetime of 45 Myr and is switched off afterwards. Each source can become active multiple times dur-

ing a simulation run. The resulting duty cycle is consistent with many observational studies which, however, set only weak constraints (Jakobsen et al. 2003; Martini 2004; Porciani et al. 2004; Cantalupo et al. 2007; Worseck et al. 2007; Kelly et al. 2010; Bolton et al. 2012; Cantalupo et al. 2012; Trainor & Steidel 2013; Borisova et al. 2016; Schmidt et al. 2017).

The fraction of active sources at $z \sim 4$ is determined by matching the amplitude of the QLF measured by Giallongo et al. (2015, see Fig. 1). Its redshift dependence, instead, is determined by adopting a ‘pure density evolution’ model, as follows. First, we assume that the shape of the QLF does not evolve (which is consistent, to first approximation, with the results in Giallongo et al. 2015). Second, we change the fraction of active sources so that to match the evolution of the emissivity at 912 Å, $\epsilon_{912}(z)$, obtained by MH after extrapolating down to $z = 12$ a collection of observational data at $z \lesssim 6$. In practice, this is done by changing the number of active sources, $N_{\text{src,active}}(L, z)$, according to the relation

$$N_{\text{src,active}}(L, z) = C(z) N_{\text{src,active}}(L, z = 4), \quad (2)$$

where

$$C(z) = \epsilon_{912}(z) / \epsilon_{912}(z = 4). \quad (3)$$

This procedure ensures that our integrated emissivity exactly matches the input used in the analytical model by MH. On average, we end up having between 120 and 400 active sources within a single simulation box, the number increasing with time.

We model the rest-frame QSO spectral energy distribution with a broken power law:

$$f(\nu) \propto \begin{cases} \nu^{\alpha_{\text{FUV}}}, & \lambda \geq \lambda_b \\ \nu^{\alpha_{\text{EUV}}}, & \lambda < \lambda_b \end{cases} \quad (4)$$

where $f(\nu)$ is the energy flux, α_{FUV} and α_{EUV} are the spectral indices in the far UV and extreme UV, respectively, and λ_b is the junction point of the two power-laws. Following Lusso et al. (2015), we assume $\lambda_b = 912$ Å and assign to each source a pair of spectral indices sampled from two Gaussian distributions with means and standard deviations corresponding to $\alpha_{\text{FUV}} = -0.61 \pm 0.01$ and $\alpha_{\text{EUV}} = -1.7 \pm 0.61$, respectively. This matches the observed spectrum of low-redshift QSOs corrected for IGM absorption.

2.2.2 Propagation of radiation

In order to model the radiation transport, we employ an upgraded version of the three-dimensional RT code RADAMESH (Cantalupo & Porciani 2011). This software implements an efficient photon-conserving ray-tracing algorithm and is designed for AMR grids. RADAMESH uses a cell-by-cell Monte Carlo scheme to sample the radiation field at each location. The temperature and ionization state of each resolution element are computed using a non-equilibrium fully-implicit chemistry solver that includes six different species (H I, H II, He I, He II, He III and e^-).

In order to limit the computational time to an acceptable amount, we artificially decouple the RT from the hydrodynamic evolution of the gas. We thus post-process the $z = 4$ snapshot of the hydro simulations with the RT code. Ionizing photons emitted from the discrete sources described in Section 2.2.1 are propagated through the simulation box. The gas density, temperature and ionization states are updated keeping into account the local photoionization, photoheating, recombination and cooling rates as well as the expansion of the Universe. However, the spatial pattern of the density fluctuations is fully determined by the $z = 4$ output of the

hydro simulation. We briefly comment on the robustness of this approximate method in the next Section.

To ensure a proper comparison with the analytical study by MH, we assume that the first QSOs light up at $z_{\text{start}} = 12$ which is compatible with the predictions of large cosmological simulations (e.g. Di Matteo et al. 2017). The RT runs are then evolved until redshift $z_{\text{end}} = 3.5$, when both hydrogen and helium are completely ionized (i.e. their neutral volume fraction is less than 10^{-5}).

We sample the radiation spectrum between 1 and 40 Ry using 50 bins logarithmically spaced within three sub intervals starting at the ionizing thresholds of H I, He I, and He II. In details, we use 10 bins between 1 and 1.81 Ry, 10 bins between 1.81 and 4 Ry, and 30 bins in the range (4, 40] Ry. Further increasing the number of bins or modifying their frequency range produces only negligible changes in the gas temperature (see Appendix B in CCP1 for a convergence test). Note that our simulations include soft X-rays that, thanks to their long mean free path, pre-heat the gas ahead of the ionization fronts. On the other hand, we neglect secondary ionizations that are expected to have only a minor impact (Shull & van Steenberg 1985; McQuinn et al. 2009; Kakiichi et al. 2017).

We have checked that extremely bright sources that are not represented in our simulation box should not introduce significant fluctuations in the distribution of the ionizing radiation. In fact, the expected number of these QSOs with a Strömgren sphere (e.g. Haiman & Cen 2001) that overlaps with the box is always much smaller than one for any realistic combination of the QSO lifetime and the ionization state of the IGM at $z \gtrsim 5$.

At late times, when the gas in the simulations is almost completely ionized, the mean free path of the most energetic photons can exceed the box size. In order to reduce the computational time, we discard the photon packets that freely traverse the box two times (at variance with CCP2 where they were replaced by a uniform background). This approximation might slightly shift our results towards higher optical depths at the very end of the EoR.

2.2.3 Post-process RT: motivations and accuracy

RT is a very computationally intensive problem. The intensity of radiation depends on seven variables (three spatial and two angular coordinates as well as time and photon energy) and the RT equation is non local. In consequence, for the current technology, coupled RT and hydrodynamic equations turn out to be too challenging to solve within large spatial domains without making simplifying assumptions. Different approaches have been followed in the literature to study the EoR. Some authors prefer to study the coupled evolution at the price of introducing crude approximations in the RT modelling (e.g. monochromatic radiation) and/or considering limited volumes (e.g. Gnedin 2014; Ocvirk et al. 2016; Aubert et al. 2015; Pawlik et al. 2017). Others employ more detailed RT algorithms at the cost of decoupling them from the hydrodynamics (e.g. Paschos et al. 2007; McQuinn et al. 2009; Rahmati et al. 2013; Compostella et al. 2013; Bauer et al. 2015; Kakiichi et al. 2016).

In this work, we follow the second approach in order to simulate a representative cosmological volume and suppress random fluctuations in the number of rare sources like QSOs. This strategy also offers us the possibility of comparing our results with the analysis of the standard EoR scenario presented in CCP1 and CCP2 using the same numerical setup.

It has been shown that decoupling the RT from the hydrodynamical response of the gas has a small impact on the models for the EoR. For instance, Meiksin & Tittley (2012) found that gas

velocities are typically altered by $\sim 1 \text{ km s}^{-1}$ while gas densities change by less than 10 per cent. Similar conclusions have been reached by employing the same codes and setup used in this work (see Appendix A in CCP1): the gas density is altered by less than ~ 5 per cent down to $z = 3.2$ with the largest deviations seen in filamentary regions around mean density. We are thus confident that our result are sufficiently robust and accurate.

3 RESULTS

In order to give a visual impression of the development of the EoR, Fig. 2 shows a series of snapshots extracted from one of our simulations and displaying the redshift evolution of different physical quantities. From left to right, columns refer to $z = 10, 8,$ and $6,$ respectively. The top panels display the baryonic overdensity $\Delta_b(x) \equiv \rho_b(x)/\bar{\rho}_b$, where $\rho_b(x)$ is the baryon density and $\bar{\rho}_b$ denotes its mean value within the box. Over plot are the projected positions of the nearby active sources, color-coded in such a way that redder colors correspond to brighter QSOs. The second row of panels illustrates changes in the gas temperature, while the last two exhibit the evolution of the H II and He III fractions, respectively. Note that, contrary to what happens in the standard scenario, hydrogen and helium get fully ionized simultaneously at a given location. When dominated by QSOs, cosmic reionization proceeds in a very inhomogeneous fashion. First, individual ionized bubbles are formed that then percolate.

This aspect is further elucidated in Fig. 3 where we show a time sequence of volume renderings of the H I ionization fronts (here defined as the regions where the local H II fraction is 50 per cent). A topological change due to the percolation transition is clearly noticeable at $z \sim 6$.

3.1 Ionized fractions

In Fig. 4, we provide a first quantitative evaluation of the impact of early QSOs on the EoR by studying the redshift evolution of the ionized volume fraction (often referred to also as the ‘volume filling factor’) for H II (x_{HII} , top panel) and He III (x_{HeIII} , bottom panel). We do not show the He II fraction here (nor we discuss it elsewhere in the paper) as it matches almost perfectly x_{HII} as a consequence of the hard radiation spectrum emitted by QSOs and the close first-ionization energies of hydrogen and helium. The solid line indicates the average over our simulations and the surrounding light shaded region denotes the corresponding rms value. The four runs are in very good agreement and the scatter among them is small. Different symbols indicate a number of observational constraints on the H II fraction (Fan et al. 2006; Totani et al. 2006; McQuinn et al. 2007; Ota et al. 2008; Ouchi et al. 2010; Mortlock et al. 2011; Ono et al. 2012; Schroeder et al. 2013; Robertson et al. 2013; Schenker et al. 2014; Pentericci et al. 2014; Tilvi et al. 2014; McGreer et al. 2015; Sobacchi & Mesinger 2015; Greig et al. 2017; Mason et al. 2018; Davies et al. 2018). This confirms that the QSO-dominated model produces enough photons to generate an EoR and keep the IGM ionized afterwards as suggested by previous analytical work. An obvious benchmark for our simulations is the MH model (dashed line) which predicts similar volume fractions. Some important differences can nevertheless be appreciated: in our simulations, reionization proceeds slower at $z \gtrsim 9$ and becomes faster at $z \lesssim 7.5$. The reason is that MH describe the ionizing photons as an uniform UV background and do not consider the precise location of the sources as well as RT effects. However, our simulated QSOs

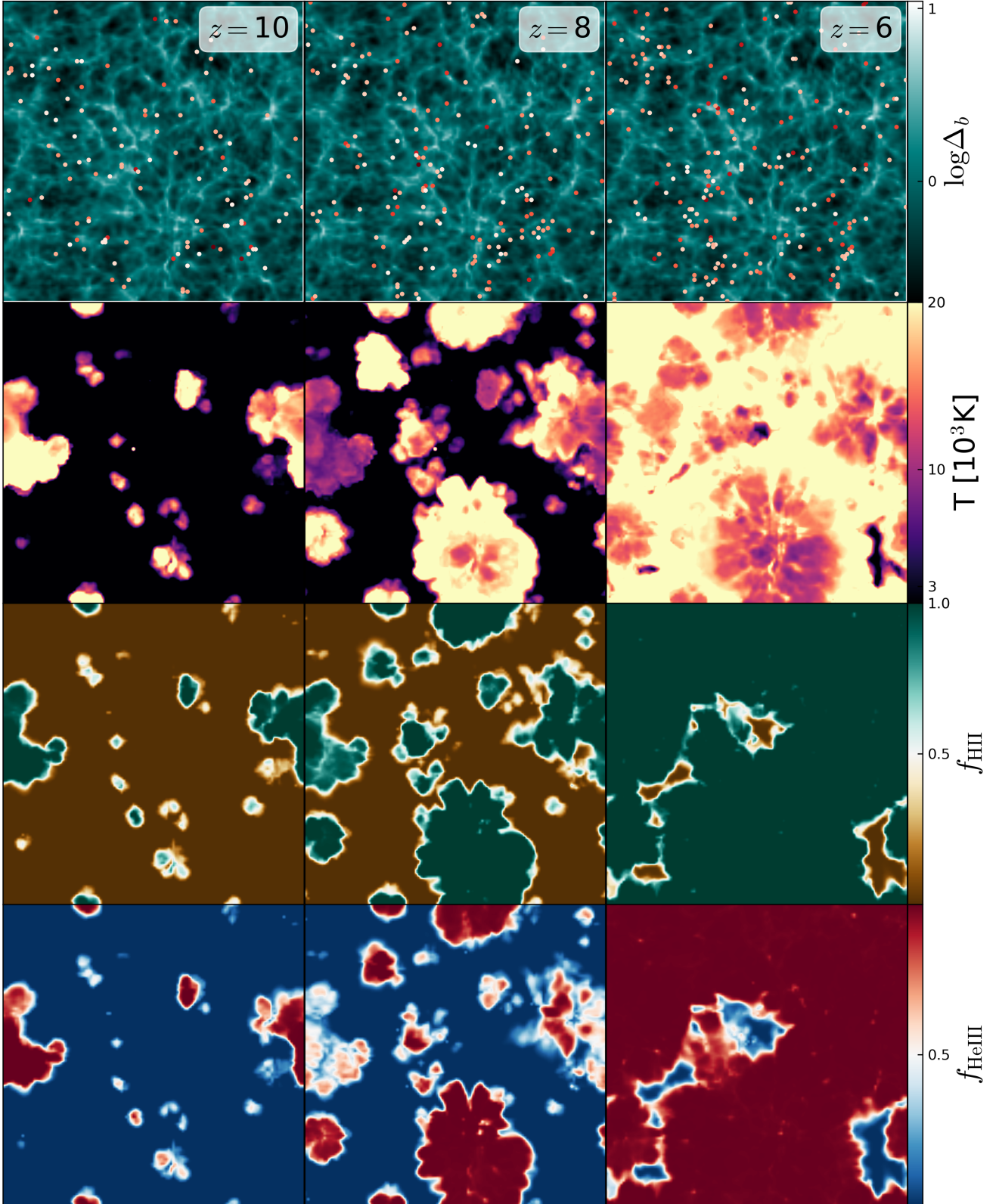


Figure 2. Simulation snapshots referring to a thin slice passing through the centre of one of our boxes. The time evolution proceeds from left to right across the frames that correspond to $z = 10, 8$ and 6 . In the top row, the baryon overdensity is shown together with the projected position of the active sources located within $\sim 4 h^{-1}$ Mpc from the slice (redder colors denote brighter sources). The second, third and fourth rows display the gas temperature as well as the H III and He III volume fractions, respectively.

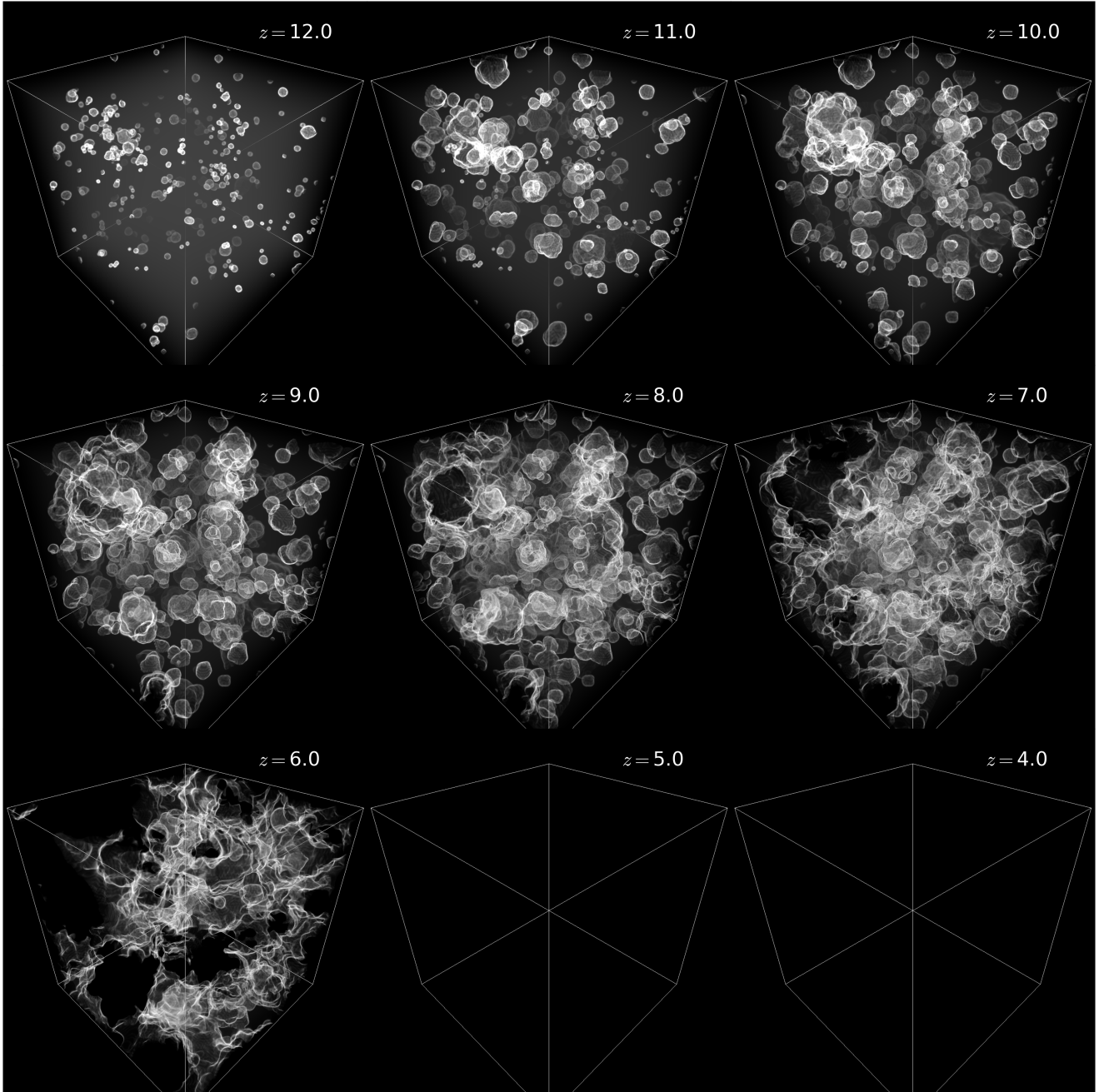


Figure 3. Volume rendering of the HI ionization front in one of our simulations at different redshifts. Neutral gas is shown in semi-transparent white, while the ionization fronts (defined as the regions where the local HII fraction is 50 per cent) are shown using opaque white.

reside in highly overdense regions of the Universe that are characterized by a faster recombination rate than average. The net effect is to slow down the progression of the reionization process around the active sources. Later on, when the overdense patches are completely ionized, the ionization fronts reach underdense regions, in which reionization takes place faster than in the analytical model.

As we have briefly mentioned above, a striking feature characterizing the QSO-dominated scenario (compared with the standard model of the EoR) is the nearly simultaneous ionization of HI and He II. This is a direct consequence of the assumption that only one population of sources provides all the ionizing photons for both

species. By directly comparing the evolution of x_{HII} and x_{HeIII} in Fig. 4, it emerges that the volume fraction of ionized hydrogen is a bit higher at all times. This small delay in the reionization of helium reflects the shape of the QSO spectrum that gives less ionizing photons per helium atom than for hydrogen (see, however, the discussion in Section 5 on the impact of the escape fraction).

The peculiar reionization histories in the QSO-only scenario modify the number density of free electrons in the IGM with respect to the standard model of the EoR. In Fig. 5, we show that the resulting optical depth of CMB radiation to Thomson scattering,

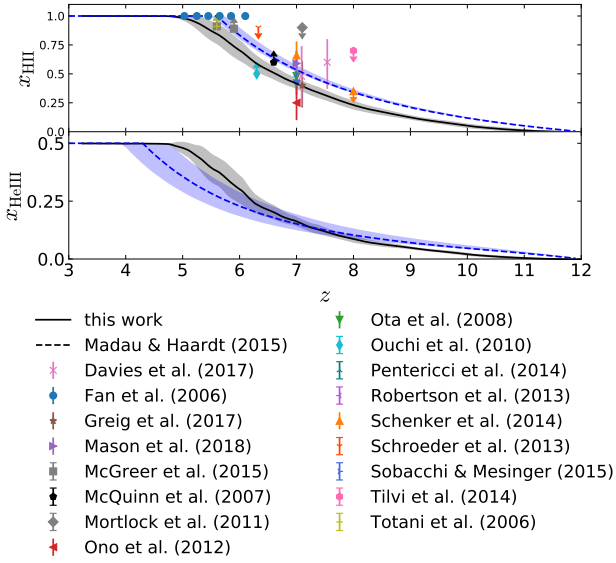


Figure 4. Volume fraction of H II (top) and He III (bottom) computed from our simulation suite. The solid lines and the surrounding shaded regions show the mean and the rms scatter among the four realizations. The dashed lines indicate the predictions by MH and the shaded areas around them describe the effect of varying the parameters of their analytical model. The symbols correspond to a collection of constraints on the hydrogen ionized fraction as indicated by the labels.

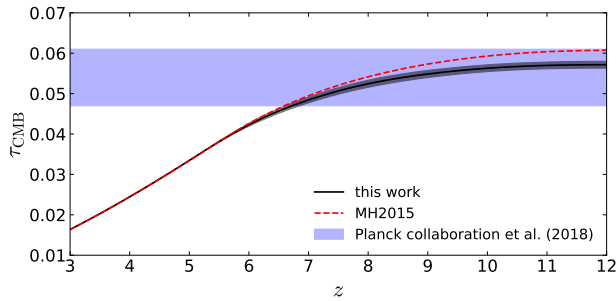


Figure 5. Optical depth to Thomson scattering integrated from the present time to redshift z . The solid line and the surrounding shaded region correspond to the results from our simulations shown in Fig. 4. The dashed curve shows the prediction by MH. The large shaded area highlights the current observational constraints for the CMB at $z \sim 1100$ (Planck Collaboration et al. 2018).

τ_{CMB} , still lies within the observational constraints (Planck Collaboration et al. 2018) as also derived by MH (dashed lines).

3.2 IGM temperature

Although analytic models of reionization can compute the ionized volume fractions rather accurately, they cannot make robust predictions for the IGM temperature which is heavily influenced by RT effects. For instance, MH assume that the IGM has a uniform temperature of $T_{\text{IGM}} = 2 \times 10^4$ K, neglecting any dependence on redshift or density. In Fig. 6, we show the redshift evolution of the gas temperature at mean density (T_0) in our simulations. The solid line and the shaded area around it denote the mean and the associated

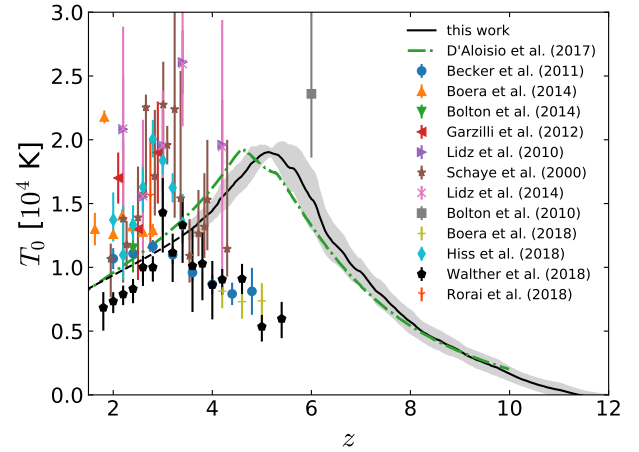


Figure 6. Volume-weighted average temperature of the IGM at mean density, T_0 , as a function of redshift. The average (solid line) and the rms scatter (shaded area) are evaluated over the entire simulation suite. For $z < 3.5$, we use an analytical approximation to extrapolate the evolution of T_0 beyond the range covered by the simulations (dashed line). The symbols show a collection of observational data (see the main text for details). The dot-dashed line represents the semi-analytical prediction by D’Aloisio et al. (2017b).

scatter among all the mean-density cells in the four realizations. For completeness, we extrapolate T_0 at $z < 3.5$ (dashed line) as in McQuinn & Upton Sanderbeck (2016) by taking into account that, when the gas is fully ionized, the temperature at mean density is determined by the adiabatic expansion of the Universe (plus smaller contributions due to Compton and free-free cooling). Overall, the IGM is photo-heated until $z \approx 5.5$ and cools down afterwards. Note that, excluding its maximum value, $T_0 \ll 2 \times 10^4$ K at all times. A similar trend was derived by D’Aloisio et al. (2017b) using semi-analytical methods (although, in their case, the peak temperature is reached a bit later, at $z \sim 4.5$, see the dot-dashed line in Fig. 6).

Several observational constraints published by various authors using substantially different methods are overplotted in Fig. 6. Namely, we show the results obtained by Schaye et al. (2000, using the distribution of line widths in the Ly α forest), Bolton et al. (2010, from the Doppler parameter in the quasar proximity zone), Becker et al. (2011, from the curvature statistic), Garzilli et al. (2012, via a wavelet filtering analysis), Bolton et al. (2014, from the distribution of line widths), Boera et al. (2014, employing the curvature statistic), Lidz & Malloy (2014, using the Morlet wavelet filter analysis), Rorai et al. (2018, from the joint distribution of HI column densities and Doppler parameters), Boera et al. (2018, using the flux power spectrum), Hiss et al. (2018, employing the cutoff in the Doppler parameter distribution) and Walther et al. (2018, using the Ly α forest power spectrum). Although statistical errorbars tend to be large and different methods do not always match, the available data show a peak around $z \approx 3.5$, which is usually interpreted as a signature of late helium reionization (e.g. McQuinn 2016, and references therein). This clearly poses a severe challenge to the QSO-dominated model which cannot accommodate such a late local maximum in $T_0(z)$. In general, it is impossible to fit the existing temperature constraints if He II reionization takes place at $z > 4.5$ (Upton Sanderbeck et al. 2016; D’Aloisio et al. 2017a).

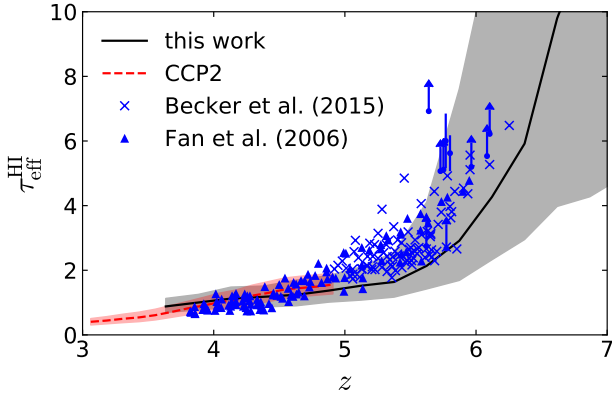


Figure 7. The redshift evolution of the HI effective optical depth computed from synthetic spectra in different numerical simulations is compared with recent observational estimates. The solid line shows the median value obtained from our simulation suite of the QSO-dominated scenario for the EoR. The corresponding evolution in the standard model of reionization (see CCP2) is displayed with a dashed line. In both cases, the shading indicates the central 68 per cent of data. The observational results by Becker et al. (2015) and Fan et al. (2006) are shown with triangles and crosses (or vertical arrows for lower limits), respectively.

4 SYNTHETIC OBSERVATIONS

The hydrogen and helium Ly α forests are powerful probes of the IGM properties. In this Section, we use our simulations of the QSO-dominated reionization model to produce synthetic absorption-line spectra for HI and He II that we then compare with observational data and previous numerical studies. Finally, we suggest new ways to analyse the experimental data and better constrain the QSO contribution to reionization.

The mock spectra are generated as in CCP1. In brief, we compute the IGM absorption profile as a function of wavelength by keeping into account the effects of density, temperature and velocity. For each simulation snapshot, we consider 100 random lines of sight, each one extending for $100 h^{-1}$ Mpc. In total, we produce ~ 12000 spectra with an initial resolution of 1 km s^{-1} that we subsequently degrade by using a Gaussian filter with a full width at half maximum of 88 km s^{-1} in order to mimic the instrumental response of an actual spectrograph. The smoothing length matches the nominal resolution of our simulations in low-density regions at $z \approx 3.5$. Although our mock spectra do not resolve individual absorption features in the Ly α forest, they do encode information about the IGM opacity.

4.1 Effective optical depths

The evolution of the effective optical depth, τ_{eff} , has emerged as one of the most widely used characterizations of the Ly α forest. In order to evaluate this statistic for our simulations, we first divide each synthetic spectrum in chunks of size $\Delta z = 0.1$ (as in e.g. Becker et al. 2013) and compute the (continuum-normalized) mean transmitted flux in it, $0 \leq \langle F \rangle \leq 1$. The effective optical depth is then obtained using $\tau_{\text{eff}} = -\ln \langle F \rangle$.

The resulting values for the HI forest are plotted in Fig. 7. The solid line shows the median value in each redshift bin and the surrounding shaded region encloses the central 68 per cent of the data. For comparison, we also display the results obtained by

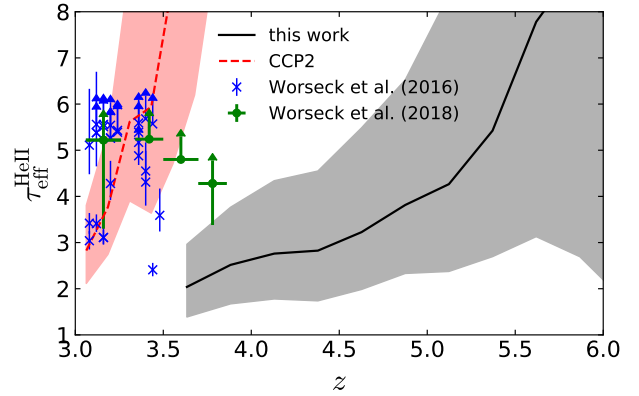


Figure 8. As in Fig. 7 but for the He II effective optical depth. The data points indicate the measurements by Worseck et al. (2016, crosses) and Worseck et al. (2016). For visual clarity only the median and 68 per cent central data within each redshift bin are shown]Worseck+2018.

CCP2 within the standard scenario for reionization (dashed line and shaded region). The large scatter seen in our simulations at $z \gtrsim 5.5$ is a clear indication of patchy reionization caused by the low number density of QSOs (see also Section 4.2). Overplotted are observational data for 42 quasar spectra (Fan et al. 2006; Becker et al. 2015). At $z \lesssim 4.5$, the simulations are in excellent agreement with the observations, especially taking into account that they should be slightly biased towards higher effective optical depths at low redshifts (see Section 2.2). On the other hand, at higher redshifts, the IGM in the simulations tends to be too transparent, with most of the observational data falling in the upper half of the synthetic distribution of $\tau_{\text{eff}}^{\text{HI}}$.

We repeat the same analysis for the He II Ly α forest but using chunks with $\Delta z = 0.04$ as in Worseck et al. (2016). The late evolution¹ of $\tau_{\text{eff}}^{\text{HeII}}$ is plotted in Fig. 8, together with recent measurements from Worseck et al. (2016) and Worseck et al. (2018, including new and re-analyzed spectra). Despite the small number of experimental data in the redshift range covered by our simulations, the model and the observations are in strong tension. In fact, the optical depths predicted by the QSO-dominated scenario at $z \approx 3.7$ are substantially lower than the observed ones at $z = 3.4$. On the contrary, the standard reionization scenario is in good agreement with the available data.

In summary, the QSO-dominated scenario we have simulated does not match the observed evolution of the IGM opacity. For what concerns HI, however, a moderate delay in the appearance of the first active sources and/or a steeper evolution of the ionizing emissivity could reduce (and likely completely remove) the small tension we have found with the data at intermediate redshifts. Conversely, it does not seem possible to reconcile the model and the

¹ In the QSO-dominated model, $\tau_{\text{eff}}^{\text{HeII}}$ changes in a peculiar way with redshift. After the first QSOs become active, He II is present only in between the hydrogen and helium ionization fronts which are generally close in space. Therefore, the effective optical depth assumes rather low values at early times ($\tau_{\text{eff}}^{\text{HeII}} \lesssim 6$) that steadily grow as the separation between the hydrogen and helium fronts increases due to the steep spectral index of the ionizing radiation. The effective optical depth reaches its maximum value around the epoch of hydrogen reionization and decreases afterwards. In fact, once the H II bubbles percolate, He II regions find themselves illuminated by multiple sources and are rapidly turned into He III.

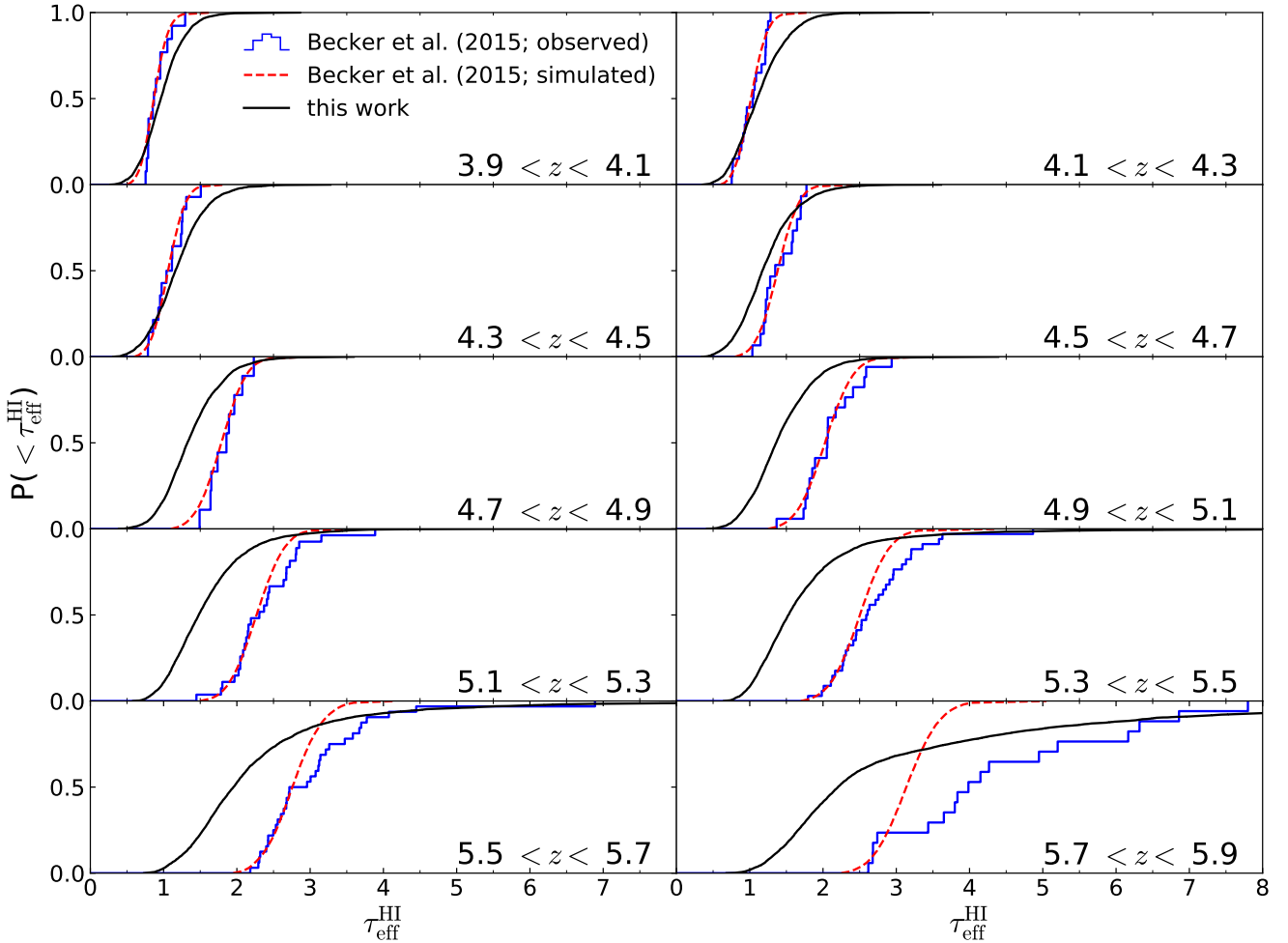


Figure 9. Cumulative distribution function of the HI effective optical depth. The solid curve shows the median over our simulations. The histogram displays the observational results by Becker et al. (2015), while the dashed curve indicates the CDF predicted using numerical simulations of a standard reionization history calibrated to match the low-optical-depth end of the observed distribution (also from Becker et al. 2015). Each panel corresponds to a different redshift bin as indicated by the labels.

data for He II by making small adjustments. Simply, helium reionization is completed too early in the QSO-dominated scenario.

4.2 The probability distribution function of optical depths

The spread in $\tau_{\text{eff}}^{\text{HI}}$ recorded at fixed redshift indicates that the opacity of the intergalactic hydrogen varies between different sightlines. The cumulative distribution function (CDF) of $\tau_{\text{eff}}^{\text{HI}}$ thus provides a simple and convenient characterization of these local changes. In Fig. 9, we plot the CDF measured by Becker et al. (2015) using spectral chunks with a comoving length of $50 h^{-1}$ Mpc. It is well known that these results, that have been recently confirmed with increased statistical significance (Bosman et al. 2018; Eilers et al. 2018), are inconsistent with the distribution inferred from numerical simulations of the standard reionization model that employ a uniform UV background² calibrated to match the observed low-

optical-depth data (see the dashed lines in Fig. 9). In fact, the CDF extracted from the simulations is too steep and can not reproduce the extended tail of large optical depths observed at redshift $z \gtrsim 5$ (Becker et al. 2015). It is thus interesting to verify whether the QSO-dominated scenario (with its rarer ionizing sources) may help reconciling the discordance with the observations. The solid lines in Fig. 9 represent the CDF obtained from our mock spectra. Before proceeding with the comparison, it is important to stress that our optical depths have not been calibrated to match any part of the observed CDF. In general, the modified scenario for the EoR does not reproduce the observations at any redshift. At $z \lesssim 4.5$, the observed CDF is steeper than the simulated one, meaning that the IGM is more homogeneous than predicted by the QSO-dominated model.

Including fainter QSOs in the simulations may relieve this tension, as a larger number density of sources can produce a more homogeneous IGM. At $4.5 \lesssim z \lesssim 5.5$, the simulated CDF has the correct shape but is systematically shifted towards lower optical depths (as already seen in Fig. 7). At even higher redshift, the disagreement increases at small optical depths but the synthetic CDF nicely reproduces the high- $\tau_{\text{eff}}^{\text{HI}}$ tails of the distribution (mainly

² Although using a smooth radiation field represents a rather crude approximation during the early phases of the EoR, it should be a sufficiently good working hypothesis after bubble percolation (i.e. at $z \lesssim 6$).

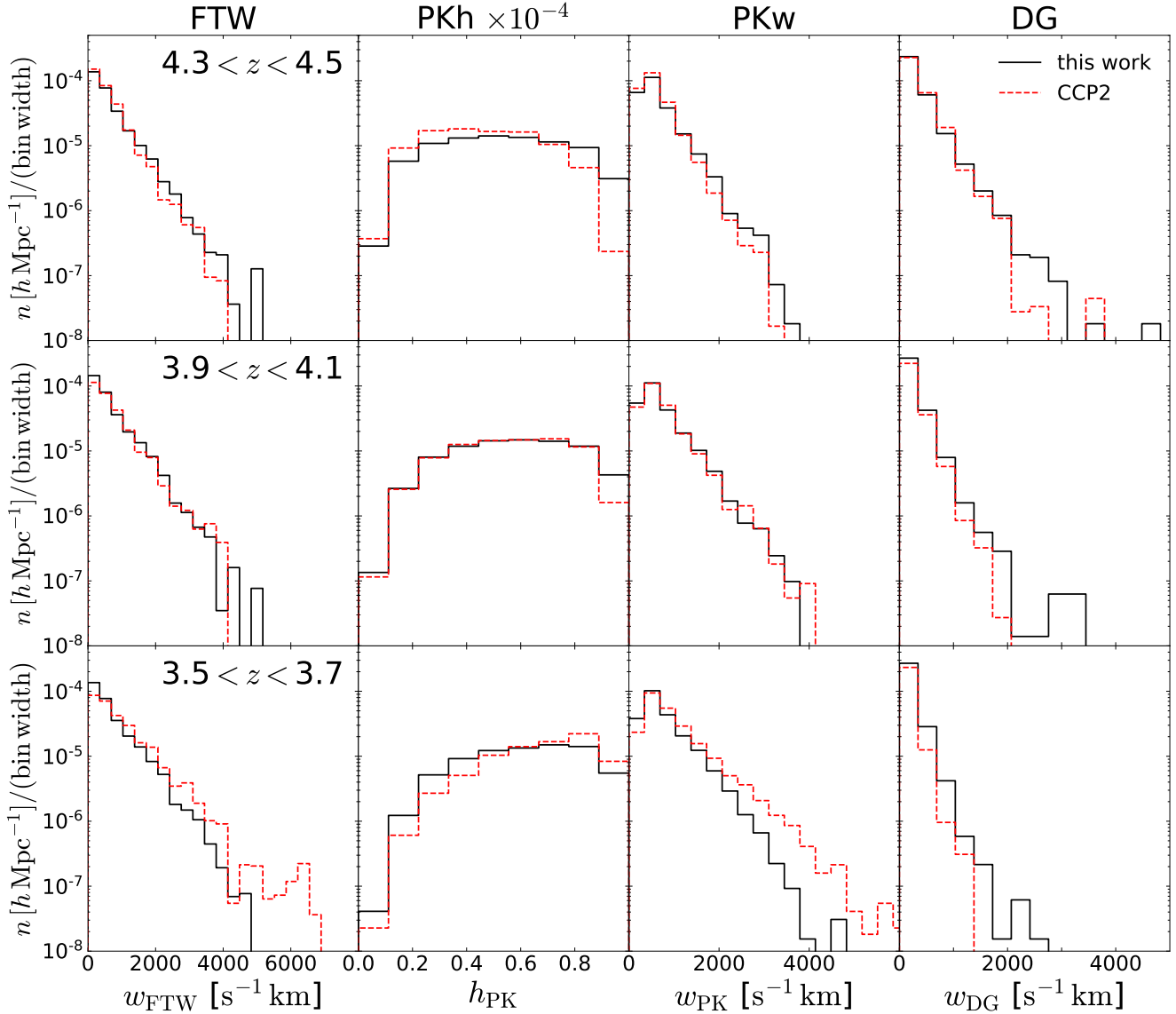


Figure 10. Distribution of shape properties of transmission peaks and dark gaps in synthetic spectra of the HI Ly α forest. Each row refers to a different redshift reported in the leftmost panel. Each column shows the density distribution along synthetic sightlines of (from left to right) the width of flux transmission windows, the height (rescaled by a factor 10^{-4} for visual clarity) and width of transmission peaks and the size of dark gaps. A precise definition of these quantities is given in the text. Solid lines show the result for our simulations while dashed lines refer to the standard reionization history and employ the simulations of CCP2.

driven by spatial fluctuations of the photoionization rate but also by the large islands of neutral hydrogen present at these redshifts). This is the opposite trend to that expected in the standard reionization model (Becker et al. 2015) unless the EoR for HI extends down to $z \sim 5.3$ (Kulkarni et al. 2018). It is therefore tempting to interpret our results as implying that an increased QSO contribution at high redshift (with respect to the standard reionization history, see also Chardin et al. 2017) might bring the theoretical predictions in agreement with observations. Dedicated numerical studies are necessary in order to settle this issue which is beyond the scope of this paper.

4.3 Statistical properties of peaks and gaps

In this Section and the next one, we use our synthetic spectra to explore possible ways of gauging the QSO contribution to cosmic reionization with observational data. We proceed by comparing the predictions of the QSO-dominated scenario with those of the standard model. For the latter, we use the results presented in CCP2. Our analysis does not involve any fine tuning of the model parameters. Moreover, the statistics discussed here may not be fully converged at the resolution achieved by our simulation suite. As such, our study is qualitative in nature. Our intention is to provide a guideline for future studies that will employ hybrid populations of ionizing sources in order to make more quantitative statements.

We first isolate specific features generated by HI and HeII

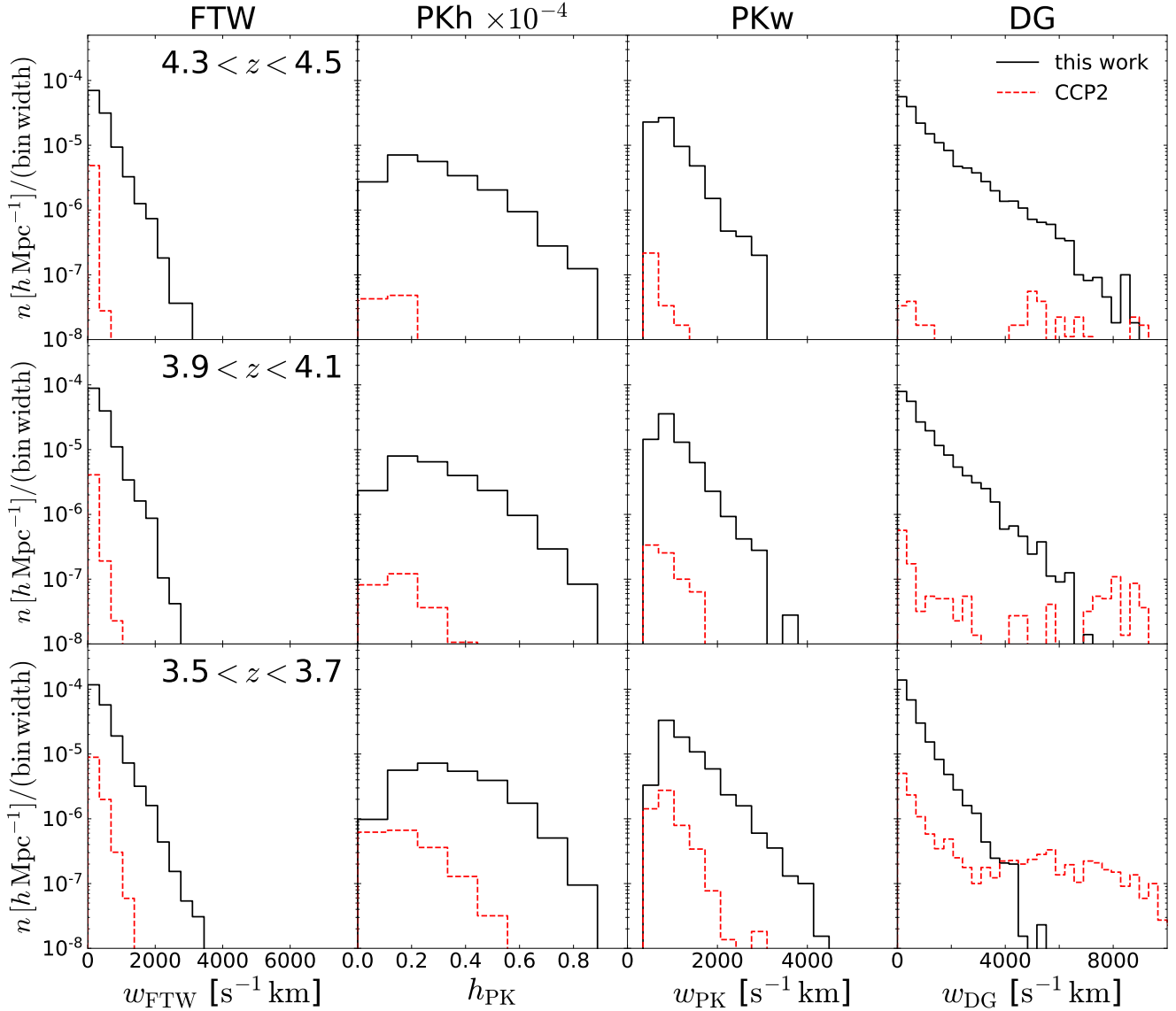


Figure 11. As in Fig. 10 but for the He II Ly α forest. Notice the different horizontal scale in the rightmost column.

Ly α absorption in QSO spectra and characterize them in terms of four numbers. Following CCP1, we consider the width of flux-transmission windows (FTW) defined as the (simply connected) regions where the transmitted flux is everywhere greater than 20 per cent of the continuum level. We also examine the length of dark gaps (DG) that are intended as the extended regions where the flux is everywhere below 10 per cent of the continuum level. Finally, we look at transmission peaks (Gallerani et al. 2008; Gnedin et al. 2017) that we define as the continuous regions where the flux always lies above a threshold value of 0.5 times the maximum transmitted flux within the segment. In particular, we record the width and the maximum height of the peaks (hereafter PKw and PKh, respectively). For this analysis, in order to avoid classifying small local fluctuations as peaks, we add Gaussian noise with an rms value of $F_{\text{noise}} = 0.05$ to the synthetic spectra and only consider peaks with a signal-to-noise ratio greater than 3.

Our results are shown in Fig. 10 for the HI Ly α forest and in

Fig. 11 for the He II spectra. In both cases, we compare the quasar-only scenario (solid lines) with the standard one as computed in CCP2 (dashed lines) and focus on $z \lesssim 4.5$. Shown are the density distributions of the different features per comoving pathlength in h^{-1} Mpc. For HI, the two models give very similar results as hydrogen is highly ionized in the post-overlap phase and the transmissivity in the spectra is mostly dictated by the underlying density field. Small deviations are noticeable at late times because the models generate different intensities of the UV background. Overall, the distribution of DG widths (w_{DG}) shifts towards shorter values as the redshift decreases (see the rightmost column in Fig. 10) as a consequence of the increasing ionization level of the IGM. Complementarily, the widths of FTWs (w_{FTW} , leftmost column) and PKs (w_{PK} , third column from the left) tend to increase. On the other hand, the distribution of peak heights (h_{PK} , second column) hardly changes with time.

The two scenarios for the EoR, however, make very different

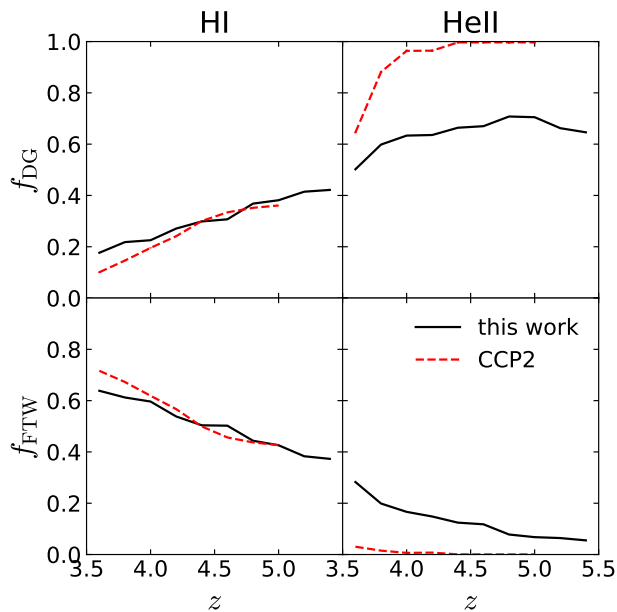


Figure 12. Average fraction of a spectrum classified as DGs (top) or FTWs (bottom) as a function of redshift. The panels on the left-hand side refer to the HI Ly α forest and those on the right-hand side to He II. The solid lines show the evolution in our set of simulations of the QSO-dominated scenario, while the dashed ones show the results of CCP2 for the standard model of the EoR. Statistical errors are always smaller than the line thickness.

predictions for the He II spectra. Because of the late reionization of He II, the standard model of reionization generates many less features than the QSO-dominated scenario. Moreover, their distributions rapidly evolve with time thus showing the opposite trend as in the QSO-dominated scenario where He II reionization takes place much earlier. It is worth noticing that, in the standard case, the widths of FTWs and PKs are usually smaller than for HI as a consequence of the reduced number of ionizing photons available. Complementarily, the width of DGs is larger. In particular, at $z \approx 3.6$, the standard scenario generates a prominent tail of very long DGs with $w_{\text{DG}} \gtrsim 4500 \text{ km s}^{-1}$ that is not present in the QSO-dominated case because of the higher number density of hard photons.

At first sight, it might be surprising that the number densities of both FTWs and DGs are small at high redshift. The reason is that our analysis equally weights long and short features, i.e. a completely absorbed spectrum will account for only one (long) DG, whilst a typical line of sight showing the Ly α forest will produce hundreds of DGs. In order to provide the missing information, in Fig. 12, we plot the evolution of the mean fraction of the spectra which is assigned to DGs (f_{DG} , top) or FTWs (f_{FTW} , bottom). As expected, the portion of the spectra which is identified as FTWs increases with time while f_{DG} decreases. Once again, results for HI are very similar in the two scenarios while they strongly differ for He II, reflecting the different timing of helium reionization. In particular, in the standard model, there is basically no transmitted flux for $z \gtrsim 4.5$ while 30 to 40 per cent of the pixels at these redshifts are not dark in the QSO-dominated scenario.

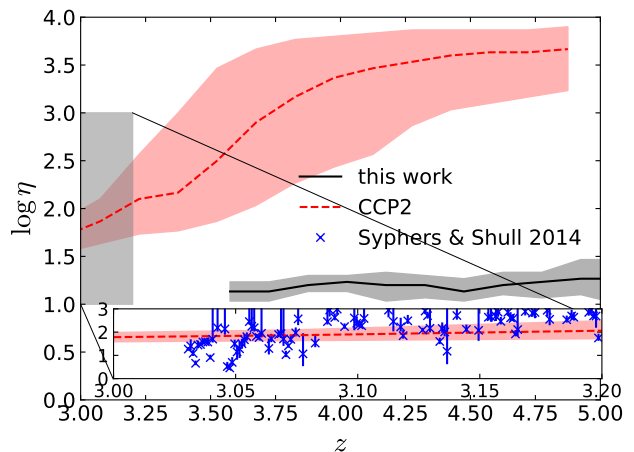


Figure 13. Percentiles of the distribution of the column density ratio, η , as a function of redshift. The lines show the median value extracted from our simulations (solid) and from those in CCP2 (dashed) while the shaded regions enclose the central 68 per cent of the data. The rectangular box on the left-hand side indicates the area containing the observational results by Syphers & Shull (2014) and is magnified in the inset for visual clarity.

4.4 The column-density ratio

An useful tool to constrain the QSO contribution is the He II-to-HI column-density ratio, η . This quantity can be measured from QSO sightlines that are transparent in the Lyman continuum because no intervening Lyman limit systems block the UV part of the spectrum (hereafter He II QSOs). For optically thin gas, the ratio encodes information on the spectral hardness of the ionizing radiation and thus on the relative contributions from hard (QSOs) and soft (stellar) sources.

In Fig. 13, we show how the probability density of η evolves as a function of redshift in our simulations and in those by CCP2. The solid lines show the median column-density ratio and the dashed lines enclose the central 68 per cent of the data. Results are very different in the standard and in the QSO-dominated scenarios due to the different timing of He reionization. In the standard model, right after hydrogen reionization is completed, η assumes values of several thousands (meaning that little or no flux is transmitted at the frequency of the He II Ly α transition) that tend to decrease with time and show a large scatter. In this case, η fluctuations mainly trace the He II density and the patchiness of He II-ionizing radiation. Later on, when also He II is fully ionized, the η distribution presents a broad peak at $\eta \sim 200$ (see also Meiksin & Tittley 2012). On the other hand, in the QSO-dominated model, HI and He II are ionized in parallel and their column-density ratio assumes significantly lower values, typically ranging between a few and a hundred at $z > 6$. As soon as the reionization of both species is completed, the PDF of η rapidly relaxes to its final form which sharply peaks at $\eta \sim 14$ and presents very little scatter.

Observations should be able to distinguish between these very different evolutionary paths and final states. Current statistical samples at $z \lesssim 2.7$ (Shull et al. 2010) provide a better match to the η -distribution generated during the standard reionization history. Consistently, rare data at higher redshifts present signs of incomplete He II reionization at $z \gtrsim 3$ (e.g. Syphers & Shull 2014). It is thus plausible that collecting more He II-absorption spectra at $z \sim 3$ and contrasting them with custom-made numerical simula-

tions might help us to precisely gauge the importance of the quasar contribution to the EoR.

5 DISCUSSION AND CONCLUSIONS

Determining the nature of the astrophysical sources of radiation that shaped the EoR continues to be an elusive goal. The tentative detection of a population of faint QSO candidates at high redshifts (Giallongo et al. 2015) led MH to investigate a scenario in which the emission from active galactic nuclei dominates over the contribution of star-forming galaxies at all times. Their analytical calculations indicate that such a model is compatible with observations of the HI volume fraction and with the optical depth to Thomson scattering of the cosmic microwave background. In this paper, we have further scrutinized the QSO-dominated scenario by using more sophisticated tools. We have run full hydrodynamical simulations and post-processed their output with a radiative-transfer code in order to compute the evolution of the temperature and ionization state of the IGM. Subsequently, we assess the viability of the QSO-dominated scenario by producing synthetic absorption-line HI and He II spectra from our simulations and comparing their properties with observations and with previous studies of the standard model for the EoR.

Our main results can be summarized as follows.

(i) The HII and HeIII volume fractions extracted from our simulations of the QSO-dominated scenario are consistent with most observational constraints and with the analytical model by MH. Similarly, the Thomson optical depth of the IGM is in very good agreement with the latest measurements (Planck Collaboration et al. 2018).

(ii) The striking feature that characterises the QSO-only scenario is that H I, He I, and He II reionization take place nearly at the same time. In consequence, the IGM temperature at mean density shows a single peak at redshift $z \approx 5.5$ (where $T_{0,\text{peak}} \approx 2 \times 10^4$ K). Compared with the bulk of the observed values, the model over predicts the IGM temperature at $4 < z < 5$ and under predicts it at $2 < z < 3$. In particular, due to the early completion of He II reionization, the QSO-dominated model is inconsistent with the measurements that show a temperature peak at $z \approx 3$. Our results are largely in agreement with the semi-analytical calculations presented by D’Aloisio et al. (2017b) although the IGM temperature peaks at an earlier time in our simulations.

(iii) Correspondingly, the effective optical depth derived from our He II Ly α synthetic spectra is significantly too low at $3 < z < 4$ to reproduce the observational constraints.

(iv) The QSO-dominated model overpredicts opacity fluctuations in the HI Ly α forest at all redshifts. When taken together, this feature, the under-estimation of the He II effective optical depth, and the temperature evolution at odds with observations, constitute a (most likely irremediable) challenge for the scenario in which AGNs fully shape the EoR.

(v) The redshift evolution of several features in the He II Ly α absorption spectra easily differentiates the QSO-dominated model for the EoR from the standard one and could be used to set tight constraints on the onset of He II reionization. Conversely, the properties of the HI Ly α forest are very similar in the two scenarios. Therefore, major progress in the field could be achieved by increasing the size of current samples of He II quasars and extending them to higher redshifts.

(vi) Although the QSO-dominated model is not able to fully reproduce the observed PDF of the HI effective optical depth at

$z \gtrsim 4.5$, it nicely generates very extended tails at high values that are not present in the standard scenario where the reionization of HI is much more spatially homogeneous and less patchy. This provides a hint that complementing the standard scenario with a sub-dominant population of high- z QSOs might be key to reconcile the observed distribution of optical depths with the predictions from numerical simulations. However, a ‘Goldilocks problem’ emerges: the QSO contribution to the EoR needs to be highly fine tuned in order to match the distribution of optical depths without generating tension with other observables.

In brief, our principal conclusion is that existing constraints on the IGM temperature and He II opacity rule out the QSO-dominated scenario we have investigated. There is a possible caveat, however. Throughout the paper, we have assumed that all UV photons escape their sources independently of wavelength. This is a common expectation motivated by the large luminosity of active galactic nuclei, although it has not been tested for the faint sources that generate most of the ionising photons at high redshift. By relaxing the hypothesis that $f_{\text{esc}} = 1$ across all (relevant) wavelengths and assuming that $f_{\text{esc}}(\sim 912 \text{ \AA}) > f_{\text{esc}}(\sim 228 \text{ \AA})$, it should be possible to delay the onset of He II reionization and vastly improve the agreement with current observational constraints on the temperature of the IGM and the He II opacity. This, however, will not modify much the PDF of the HI optical depth which is mainly influenced by radiation close to the hydrogen ionization threshold. Nevertheless, this distribution is also sensitive to sub-dominant contributions to the ionizing flux and dedicated simulations including also variable levels of stellar UV radiation need to be performed to address this issue in a more quantitative way.

Our results suggest that a rather extreme fine tuning of the escape fraction might be necessary to bring the QSO-dominated model for the EoR in agreement with existing observational data. Our analysis also reveals that developing a fully quantitative understanding of populations of sources that are active in the different phases of the EoR requires that future observational campaigns will collect many more He II QSO spectra so that to enable statistical studies of their characteristic features.

ACKNOWLEDGEMENTS

We thank Emanuele Giallongo, Andrea Grazian, Frederick Davies and the anonymous referee for useful comments. This work is carried out within the Collaborative Research Centre 956 ‘The Conditions and Impact of Star Formation’, sub-project C4, funded by the Deutsche Forschungsgemeinschaft (DFG). We are thankful to the community developing and maintaining software packages extensively used in our work, namely: Matplotlib (Hunter 2007), NumPy (Walt et al. 2011), SciPy (Jones et al. 2001), yt (Turk et al. 2011).

REFERENCES

- Aubert D., Deparis N., Ocvirk P., 2015, *MNRAS*, **454**, 1012
- Bañados E., Venemans B., Walter F., Kurk J., Overzier R., Ouchi M., 2013, *ApJ*, **773**, 178
- Barnett R., Warren S. J., Becker G. D., Mortlock D. J., Hewett P. C., McMahon R. G., Simpson C., Venemans B. P., 2017, *A&A*, **601**, A16
- Bauer A., Springel V., Vogelsberger M., Genel S., Torrey P., Sijacki D., Nelson D., Hernquist L., 2015, *MNRAS*, **453**, 3593
- Becker G. D., Bolton J. S., Haehnelt M. G., Sargent W. L. W., 2011, *MNRAS*, **410**, 1096

- Becker G. D., Hewett P. C., Worseck G., Prochaska J. X., 2013, *MNRAS*, **430**, 2067
- Becker G. D., Bolton J. S., Madau P., Pettini M., Ryan-Weber E. V., Venemans B. P., 2015, *MNRAS*, **447**, 3402
- Becker G. D., Davies F. B., Furlanetto S. R., Malkan M. A., Boera E., Douglas C., 2018, preprint, ([arXiv:1803.08932](https://arxiv.org/abs/1803.08932))
- Bertschinger E., 2001, *ApJS*, **137**, 1
- Boera E., Murphy M. T., Becker G. D., Bolton J. S., 2014, *MNRAS*, **441**, 1916
- Boera E., Becker G. D., Bolton J. S., Nasir F., 2018, preprint, ([arXiv:1809.06980](https://arxiv.org/abs/1809.06980))
- Bolton J. S., Becker G. D., Wyithe J. S. B., Haehnelt M. G., Sargent W. L. W., 2010, *MNRAS*, **406**, 612
- Bolton J. S., Becker G. D., Raskutti S., Wyithe J. S. B., Haehnelt M. G., Sargent W. L. W., 2012, *MNRAS*, **419**, 2880
- Bolton J. S., Becker G. D., Haehnelt M. G., Viel M., 2014, *MNRAS*, **438**, 2499
- Borisova E., Lilly S. J., Cantalupo S., Prochaska J. X., Rakic O., Worseck G., 2016, *ApJ*, **830**, 120
- Bosman S. E. I., Fan X., Jiang L., Reed S. L., Matsuoka Y., Becker G. D., Haehnelt M. G., 2018, preprint, ([arXiv:1802.08177](https://arxiv.org/abs/1802.08177))
- Cantalupo S., Porciani C., 2011, *MNRAS*, **411**, 1678
- Cantalupo S., Lilly S. J., Porciani C., 2007, *ApJ*, **657**, 135
- Cantalupo S., Lilly S. J., Haehnelt M. G., 2012, *MNRAS*, **425**, 1992
- Chardin J., Puchwein E., Haehnelt M. G., 2017, *MNRAS*, **465**, 3429
- Compostella M., Cantalupo S., Porciani C., 2013, *MNRAS*, **435**, 3169
- Compostella M., Cantalupo S., Porciani C., 2014, *MNRAS*, **445**, 4186
- D'Aloisio A., McQuinn M., Trac H., 2015, *ApJ*, **813**, L38
- D'Aloisio A., Upton Sanderbeck P. R., McQuinn M., Trac H., Shapiro P. R., 2017a, *MNRAS*, **468**, 4691
- D'Aloisio A., Upton Sanderbeck P. R., McQuinn M., Trac H., Shapiro P. R., 2017b, *MNRAS*, **468**, 4691
- Davies F. B., Furlanetto S. R., 2016, *MNRAS*, **460**, 1328
- Davies F. B., et al., 2018, *ApJ*, **864**, 142
- Di Matteo T., Croft R. A. C., Feng Y., Waters D., Wilkins S., 2017, *MNRAS*, **467**, 4243
- Eilers A.-C., Davies F. B., Hennawi J. F., 2018, preprint, ([arXiv:1807.04229](https://arxiv.org/abs/1807.04229))
- Eisenstein D. J., Hut P., 1998, *ApJ*, **498**, 137
- Fan X., et al., 2006, *AJ*, **132**, 117
- Fanidakis N., Macciò A. V., Baugh C. M., Lacey C. G., Frenk C. S., 2013, *MNRAS*, **436**, 315
- Furlanetto S. R., Dixon K. L., 2010, *ApJ*, **714**, 355
- Furusawa H., et al., 2016, *ApJ*, **822**, 46
- Gallerani S., Ferrara A., Fan X., Choudhury T. R., 2008, *MNRAS*, **386**, 359
- Garzilli A., Bolton J. S., Kim T.-S., Leach S., Viel M., 2012, *MNRAS*, **424**, 1723
- Giallongo E., et al., 2015, *A&A*, **578**, A83
- Gnedin N. Y., 2014, *ApJ*, **793**, 29
- Gnedin N. Y., Becker G. D., Fan X., 2017, *ApJ*, **841**, 26
- Greig B., Mesinger A., Haiman Z., Simcoe R. A., 2017, *MNRAS*, **466**, 4239
- Haiman Z., Cen R., 2001, in Umemura M., Susa H., eds, *Astronomical Society of the Pacific Conference Series Vol. 222, The Physics of Galaxy Formation*. p. 101
- Hassan S., Davé R., Mitra S., Finlator K., Ciardi B., Santos M. G., 2018, *MNRAS*, **473**, 227
- Hiss H., Walther M., Hennawi J. F., Oñorbe J., O'Meara J. M., Rorai A., Lukić Z., 2018, *ApJ*, **865**, 42
- Hunter J. D., 2007, *Computing In Science & Engineering*, **9**, 90
- Jakobsen P., Jansen R. A., Wagner S., Reimers D., 2003, *A&A*, **397**, 891
- Jenkins A., Frenk C. S., White S. D. M., Colberg J. M., Cole S., Evrard A. E., Couchman H. M. P., Yoshida N., 2001, *MNRAS*, **321**, 372
- Jones E., Oliphant T., Peterson P., et al., 2001, *SciPy: Open source scientific tools for Python*, <http://www.scipy.org/>
- Kakiichi K., Dijkstra M., Ciardi B., Graziani L., 2016, *MNRAS*, **463**, 4019
- Kakiichi K., Graziani L., Ciardi B., Meiksin A., Compostella M., Eide M. B., Zaroubi S., 2017, *MNRAS*, **468**, 3718
- Kelly B. C., Vestergaard M., Fan X., Hopkins P., Hernquist L., Siemiginowska A., 2010, *ApJ*, **719**, 1315
- Kim S., et al., 2009, *ApJ*, **695**, 809
- Kulkarni G., Choudhury T. R., Puchwein E., Haehnelt M. G., 2017, *MNRAS*, **469**, 4283
- Kulkarni G., Keating L. C., Haehnelt M. G., Bosman S. E. I., Puchwein E., Chardin J., Aubert D., 2018, preprint, ([arXiv:1809.06374](https://arxiv.org/abs/1809.06374))
- Lidz A., Malloy M., 2014, *ApJ*, **788**, 175
- Lusso E., Worseck G., Hennawi J. F., Prochaska J. X., Vignali C., Stern J., O'Meara J. M., 2015, *MNRAS*, **449**, 4204
- Madau P., Haardt F., 2015, *ApJ*, **813**, L8
- Martini P., 2004, *Coevolution of Black Holes and Galaxies*, p. 169
- Mason C. A., Treu T., Dijkstra M., Mesinger A., Trenti M., Pentericci L., de Barros S., Vanzella E., 2018, *ApJ*, **856**, 2
- Mazzucchelli C., Bañados E., Decarli R., Farina E. P., Venemans B. P., Walter F., Overzier R., 2017, *ApJ*, **834**, 83
- McGreer I. D., Mesinger A., D'Odorico V., 2015, *MNRAS*, **447**, 499
- McGreer I. D., Fan X., Jiang L., Cai Z., 2018, *AJ*, **155**, 131
- McQuinn M., 2016, *ARA&A*, **54**, 313
- McQuinn M., Upton Sanderbeck P. R., 2016, *MNRAS*, **456**, 47
- McQuinn M., Hernquist L., Zaldarriaga M., Dutta S., 2007, *MNRAS*, **381**, 75
- McQuinn M., Lidz A., Zaldarriaga M., Hernquist L., Hopkins P. F., Dutta S., Faucher-Giguère C.-A., 2009, *ApJ*, **694**, 842
- Meiksin A., Tittley E. R., 2012, *MNRAS*, **423**, 7
- Mitra S., Choudhury T. R., Ferrara A., 2018, *MNRAS*, **473**, 1416
- Morselli L., et al., 2014, *A&A*, **568**, A1
- Mortlock D. J., et al., 2011, *Nature*, **474**, 616
- Ocvirk P., et al., 2016, *MNRAS*, **463**, 1462
- Ono Y., et al., 2012, *ApJ*, **744**, 83
- Onoue M., et al., 2017, *ApJ*, **847**, L15
- Onoue M., et al., 2018, *PASJ*, **70**, S31
- Ota K., et al., 2008, *ApJ*, **677**, 12
- Ota K., et al., 2010, *ApJ*, **722**, 803
- Ota K., et al., 2018, *ApJ*, **856**, 109
- Ouchi M., et al., 2010, *ApJ*, **723**, 869
- Parsa S., Dunlop J. S., McLure R. J., 2018, *MNRAS*, **474**, 2904
- Paschos P., Norman M. L., Bordner J. O., Harkness R., 2007, preprint, ([arXiv:0711.1904](https://arxiv.org/abs/0711.1904))
- Pawlik A. H., Rahmati A., Schaye J., Jeon M., Dalla Vecchia C., 2017, *MNRAS*, **466**, 960
- Pentericci L., et al., 2011, *ApJ*, **743**, 132
- Pentericci L., et al., 2014, *ApJ*, **793**, 113
- Planck Collaboration et al., 2016a, *A&A*, **594**, A13
- Planck Collaboration et al., 2016b, *A&A*, **596**, A107
- Planck Collaboration et al., 2018, preprint, ([arXiv:1807.06209](https://arxiv.org/abs/1807.06209))
- Porciani C., Magliocchetti M., Norberg P., 2004, *MNRAS*, **355**, 1010
- Qin Y., et al., 2017, *MNRAS*, **472**, 2009
- Rahmati A., Pawlik A. H., Raičević M., Schaye J., 2013, *MNRAS*, **430**, 2427
- Ricci F., Marchesi S., Shankar F., La Franca F., Civano F., 2017, *MNRAS*, **465**, 1915
- Robertson B. E., et al., 2013, *ApJ*, **768**, 71
- Rorai A., Carswell R. F., Haehnelt M. G., Becker G. D., Bolton J. S., Murphy M. T., 2018, *MNRAS*, **474**, 2871
- Sadoun R., Zheng Z., Miralda-Escudé J., 2017, *ApJ*, **839**, 44
- Schaye J., Theuns T., Rauch M., Efstathiou G., Sargent W. L. W., 2000, *MNRAS*, **318**, 817
- Schenker M. A., Ellis R. S., Konidaris N. P., Stark D. P., 2014, *ApJ*, **795**, 20
- Schmidt T. M., Worseck G., Hennawi J. F., Prochaska J. X., Crighton N. H. M., 2017, *ApJ*, **847**, 81
- Schroeder J., Mesinger A., Haiman Z., 2013, *MNRAS*, **428**, 3058
- Shibuya T., Kashikawa N., Ota K., Iye M., Ouchi M., Furusawa H., Shimasaku K., Hattori T., 2012, *ApJ*, **752**, 114
- Shull J. M., van Steenberg M. E., 1985, *ApJ*, **298**, 268
- Shull J. M., France K., Danforth C. W., Smith B., Tumlinson J., 2010, *ApJ*, **722**, 1312
- Silk J., Rees M. J., 1998, *A&A*, **331**, L1

- Sobacchi E., Mesinger A., 2015, *MNRAS*, **453**, 1843
- Syphers D., Shull J. M., 2014, *ApJ*, **784**, 42
- Teyssier R., 2002, *A&A*, **385**, 337
- Tilvi V., et al., 2014, *ApJ*, **794**, 5
- Totani T., Kawai N., Kosugi G., Aoki K., Yamada T., Iye M., Ohta K., Hattori T., 2006, *PASJ*, **58**, 485
- Trainor R., Steidel C. C., 2013, *ApJ*, **775**, L3
- Turk M. J., Smith B. D., Oishi J. S., Skory S., Skillman S. W., Abel T., Norman M. L., 2011, *The Astrophysical Journal Supplement Series*, **192**, 9
- Upton Sanderbeck P. R., D'Aloisio A., McQuinn M. J., 2016, *MNRAS*, **460**, 1885
- Volonteri M., Rees M. J., 2006, *ApJ*, **650**, 669
- Walt S. v. d., Colbert S. C., Varoquaux G., 2011, *Computing in Science & Engineering*, **13**, 22
- Walther M., Oñorbe J., Hennawi J. F., Lukić Z., 2018, preprint, ([arXiv:1808.04367](https://arxiv.org/abs/1808.04367))
- Worseck G., Fechner C., Wisotzki L., Dall'Aglio A., 2007, *A&A*, **473**, 805
- Worseck G., et al., 2011, *ApJ*, **733**, L24
- Worseck G., Prochaska J. X., Hennawi J. F., McQuinn M., 2016, *ApJ*, **825**, 144
- Worseck G., Davies F. B., Hennawi J. F., Prochaska J. X., 2018, preprint, ([arXiv:1808.05247](https://arxiv.org/abs/1808.05247))
- Wyithe J. S. B., Loeb A., 2002, *ApJ*, **581**, 886
- Zaroubi S., 2013, in Wiklind T., Mobasher B., Bromm V., eds, *Astrophysics and Space Science Library* Vol. 396, *The First Galaxies*. p. 45 ([arXiv:1206.0267](https://arxiv.org/abs/1206.0267)), doi:10.1007/978-3-642-32362-1_2

This paper has been typeset from a $\text{\TeX}/\text{\LaTeX}$ file prepared by the author.